Bulletin of the Seismological Society of America, Vol. 107, No. 1, pp. 387–402, February 2017, doi: 10.1785/0120160090

Fracture Alignments in Marine Sediments Off Vancouver Island from *Ps* Splitting Analysis

by Takashi Tonegawa, Koichiro Obana, Yojiro Yamamoto, Shuichi Kodaira, Kelin Wang, Michael Riedel, Honn Kao, and George Spence

Abstract Alignments of fractures and cracks in marine sediments may be controlled by various mechanisms such as horizontal compaction and extension and basement faulting. The orientation of these alignments can be estimated through analyses of *S*-wave splitting. If sensors in ocean-bottom observations are deployed through free fall, sensor orientation needs to be determined in order for the recorded data to be used for such analyses. Here, we estimate the sensor orientation from the linear particle motions of *P*-to-*s* (*Ps*) phases converted at the sediment–basement interface and also from *T* waves that are excited by earthquakes and propagate in the seawater. We examine waveforms of local earthquakes recorded by 32 ocean-bottom seismometers (OBSs) that were deployed through free fall for three months in 2010 off Vancouver Island where the strike-slip Nootka fault zone (NFZ) intersects the deformation front of the Cascadia subduction zone. Because the particle motion of the *Ps* wave was corrected by estimating splitting parameters, the fast polarization direction, which reflects *S*-wave anisotropic structure within the sediment, can also be evaluated. Consequently, we could estimate the fast polarization direction at OBSs deployed near the NFZ and west of the deformation front. The obtained fast directions appeared to correspond to alignments of shear fractures in the marine sediments associated with the left-lateral motion of the fault in the basement along the NFZ, margin-normal cracks due to horizontal compression west of and slightly away from the deformation front, and frontal thrust faults within the accretionary prism near the deformation front.

Introduction

The left-lateral Nootka fault zone (NFZ) off Vancouver Island (Fig. 1) intersecting the northern Cascadia subduction zone developed as a result of the fragmentation of the Juan de Fuca plate at 3–4 Ma (e.g., Riddihough, 1984; Braunmiller and Nábělek, 2002). This fault zone is currently the boundary between the Explorer microplate and Juan de Fuca plate (Fig. 1a; Hyndman *et al.*, 1979). Both plates subduct beneath the North American plate, accreting marine sediments of the Cascadia basin to the continental margin. Seismic survey results indicate significant differences in the sediment structure between the two sides of the Cascadia deformation front. Normal faults are present in the Cascadia basin (e.g., Nedimović *et al.*, 2009), whereas margin-parallel thrusts and folds have formed in the accretionary prism (e.g., Yuan *et al.*, 1994). The structural fabrics can be evaluated by determining the anisotropic structure of the sediments; fast polarization of the *S* wave is expected to be in the general direction of cracks, fractures, and faults. The anisotropic structure of marine sediments can be estimated using ocean-bottom seismometers (OBSs).

From July to September 2010, the Seafloor Earthquake Array–Japan–Canada Cascadia Experiment (SeaJade) project (e.g., Scherwath *et al.*, 2011) deployed 32 OBSs off Vancouver Island with a station spacing of 15–20 km (Fig. 1a). The horizontal orientations of the OBSs, which contain gimbal-mounted short-period sensors (4.5 Hz) with three components, are unknown because they were deployed through free fall. Using the travel times of local earthquakes recorded by these OBSs, Obana *et al.* (2015) determined the locations of about 1200 earthquakes that occurred during the observation period (Fig. 1). Their results showed high-seismic activity in the NFZ but low activity in the Cascadia basin and along the northern Cascadia subduction zone. These results confirmed what had been deduced from previous land-based seismic monitoring, but with higher reliability.

If sensor orientation information can be obtained, additional waveform-based analyses can be performed, particularly by employing *S* waves and surface waves. For broadband OBSs, the horizontal orientation of the instruments can be determined using several kinds of seismic waves, including *P* waves (Wolfe *et al.*, 2009; Leahy *et al.*, 2010; Stachnik *et al.*,

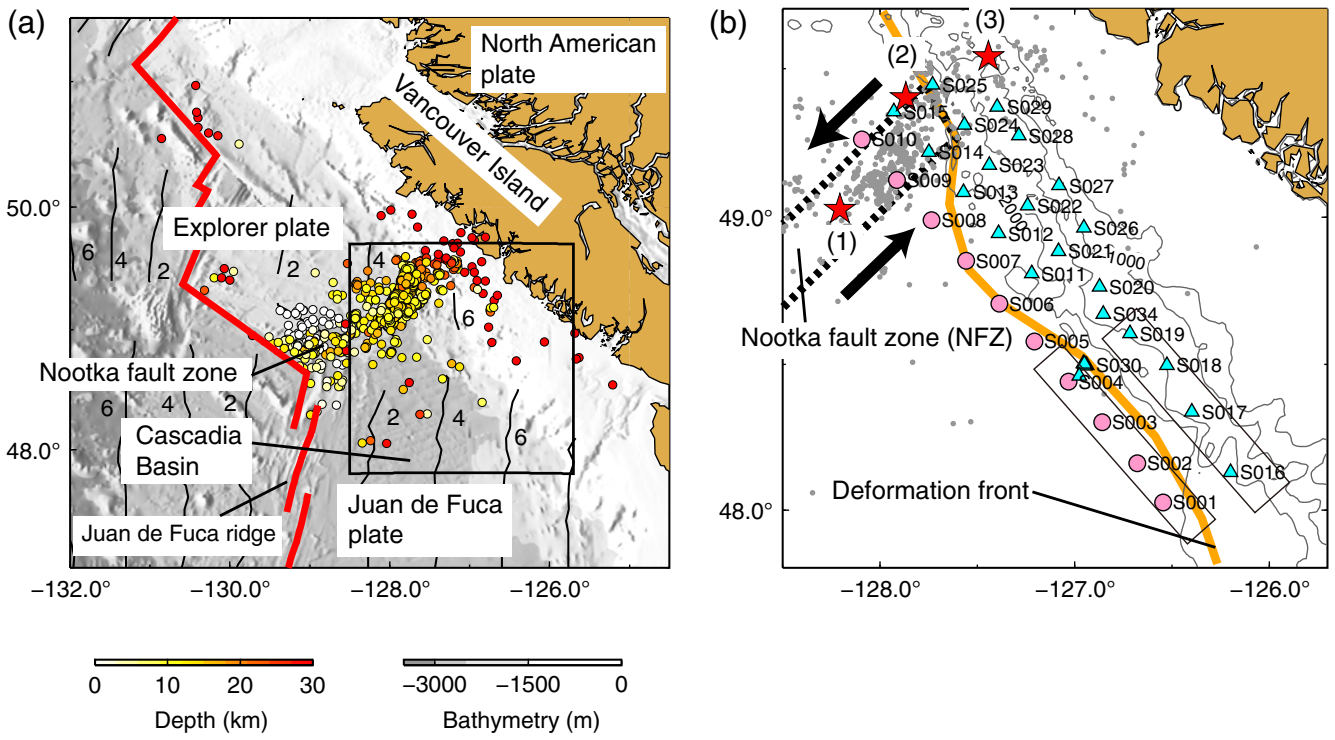

Figure 1. Maps showing the near-field earthquakes and ocean-bottom seismometers (OBSs) used in this study. (a) Locations of near-field earthquakes with known focal depths (Obana *et al.*, 2015). Bathymetry is from Smith and Sandwell (1997). Bold lines show locations of ridges and fracture zones (Bird, 2003). Numbered solid lines represent seafloor age in megaanum (Müller *et al.*, 2008). (b) The area within the box in (a) showing locations of OBSs (circles and triangles) and near-field earthquakes (gray circles). The locations of the earthquakes were determined by Obana *et al.* (2015). Stars (1)–(3) indicate the three events presented in Figure 3. Noise records from the OBSs in the two boxes are used in Figure 4. The area between the two dotted lines represents the Nootka fault zone (NFZ). Left-lateral motion of the fault zone is indicated by the arrows. The northwest–southeast-trending thick line shows the deformation front. The color version of this figure is available only in the electronic edition. The color version of this figure is available only in the electronic edition.

2012) and Rayleigh waves (Stachnik *et al.*, 2012) from teleseismic events, and Rayleigh waves from ambient noise correlation (Zha *et al.*, 2013). Using airgun shots for seafloor observation, the horizontal orientation of both short-period and broadband OBSs can be estimated from the locations of sources and OBSs (Duennebier *et al.*, 1987; Haacke and Westbrook, 2006; Haacke *et al.*, 2009; Tsuji *et al.*, 2011; Fujie *et al.*, 2013). However, because the SeaJade observations are based on short-period sensors without airgun shot records, the above methods cannot be applied. For the SeaJade project, Shan *et al.* (2012) determined the horizontal orientation of OBSs using *T* phases that are generated by earthquakes near the coast and propagate within seawater. Because the particle motion of the *T* phase, which emerges in the two horizontal components of OBSs, is almost linear and its direction corresponds to that from the source to the OBS, the sensor orientation can be estimated. However, this technique has an ambiguity of π in the estimated sensor orientation because of the unclear onset and polarity of the *T* phase.

In this article, we introduce a three-step method for determining the horizontal orientation of an OBS using *P*-to-*s* (*Ps*) waves from near-field earthquakes converted at the sediment–basement interface (Fig. 2a). We estimate the splitting parameters of the *Ps* waves so that the anisotropic structures within the sediment can also be evaluated.

Seismic Observation

From the ~1200 earthquakes reported by Obana *et al.* (2015), we selected waveforms showing both a clear *P* wave in the vertical component and a *Ps*-converted wave in the two horizontal components at 2–8 Hz frequencies. We then hand-picked the arrival times of the two waves. As a result, a total of 1732 waveform sets were collected from all available OBSs. In subsequent sections, we describe the characteristics of the observed *P* and *Ps* waves as well as the selection of events relevant to *P* waveforms.

P-Wave Observation

Recording of sufficient waveforms depended primarily on the locations of the deployed OBSs. The OBSs in the northern part of the array recorded a sufficient number of clear waveforms of *P* waves from small- and moderate-sized earthquakes that occurred near the NFZ. In the southern part of the array, clear *P* waves were recorded by several OBSs west of the deformation front, but not east of it on the accretionary

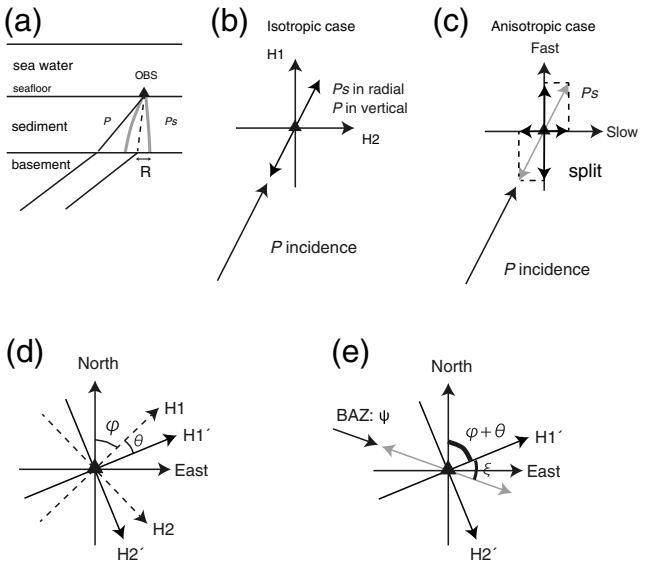

Figure 2. Geometry of ray paths of *P*- and *Ps*-converted waves and their coordinates. (a) Ray paths of the *P* wave and *Ps* wave converted at the sediment–basement interface. The label *R* indicates the horizontal radius of the sensitivity region at the sediment–basement interface. (b) Azimuthal relation between *P* and *Ps* waves in an isotropic medium and the horizontal components of OBS, H1, and H2. (c) *Ps* waves split from the *P* incidence direction to the fast and slow polarization directions. (d) Geometry of the horizontal components H1 and H2 (dashed arrows) and their rotated components H1′ and H2′ (solid arrows). The directions of H1 and H1′ are defined by φ (unknown) and $\varphi + \theta$ (fast or slow axis), respectively. (e) Back azimuth (BAZ) and the angle between H1′ and linear particle motion (gray arrow) are defined by ψ and ξ, respectively.

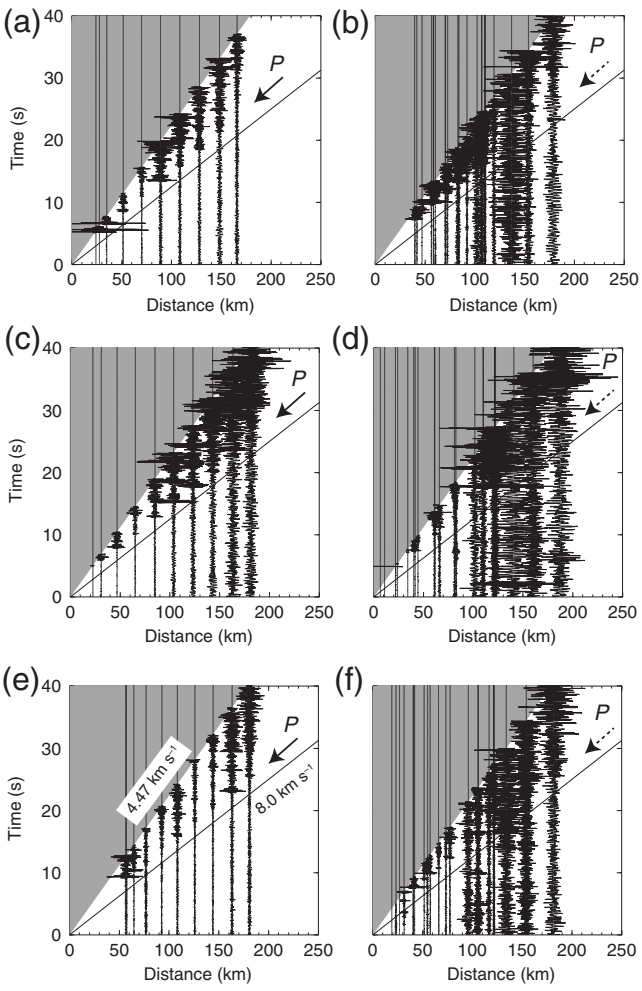

Figure 3. Waveform examples at 2–8 Hz frequencies. (a) Waveforms in the vertical component for an earthquake of magnitude 3.3 that occurred at location (1) in Figure 1b on 29 July 2010, 18:20. These waveforms were recorded at the OBSs indicated by circles in Figure 1b. Amplitudes of waves slower than 4.47 km s^{-1} are muted and masked by the gray color. (b) Same as (a) but for the OBSs indicated by the triangles in Figure 1b. (c,d) Same as (a,b) but for an earthquake of magnitude 3.0 that occurred at location (2) in Figure 1b on 9 July 2010, 16:01. (e,f) Same as (a,b) but for an earthquake of magnitude 3.5 that occurred at location (3) in Figure 1b on 14:07 24 August 2010.

prism. Figure 3 compares *P* waveforms at OBSs west and east of the deformation front for three earthquakes that occurred in the NFZ. The *P* waves reached the southern part of the array west of the deformation front but did not reach OBSs on the accretionary prism and more than 100 km away.

Figure 4 shows the normalized amplitudes of noise spectra at eight OBSs in the southern part of the array (Fig. 1b). The noise spectra were calculated from seafloor acceleration, which were converted from the seafloor velocity observed at the OBSs for a duration of 600 s (10 min), and then averaged over a 5-day period (10–14 July 2010). Because instrumental response was not known, we took the logarithm of raw amplitudes in the digital count at each OBS and normalized them with the maximum logarithmic amplitude of all the eight OBSs. As a result, at 2–8 Hz frequencies, the noise level in the accretionary prism is significantly higher than west of the deformation front, except for at one OBS site.

The reasons why few *P* waves and such high noise levels were observed on the accretionary prism remain unclear. One possibility is that the background wavefield at this frequency band (2–8 Hz) in the accretionary prism is dominated by acoustically coupled Rayleigh waves (Ewing *et al.*, 1957). These Rayleigh waves mainly propagate in the ocean-crust system and are excited by fluid disturbances (Longuet-Higgins, 1950; Kibblewhite and Evans, 1986) and/or by small-sized earthquakes as reported for the Nankai subduction zone of Japan (Tonegawa, Fukao, Takahashi, *et al.*, 2015). In the ambient seafloor noise observed in the vertical component of OBSs, the acoustic wave propagating within the seawater is dominant at frequencies higher than 5 Hz (e.g., Butler, 2006), whereas Rayleigh waves propagating mainly in the solid earth due to microseisms were observed at frequencies lower than 0.2 Hz (e.g., Webb, 1998). The acoustic Rayleigh wave is a coupled wave that propagates in seawater and sediment and is dominant in seafloor noise at frequencies between the acoustic wave and Rayleigh wave. The relatively high noise level east of the deformation front may indicate that acoustic Rayleigh

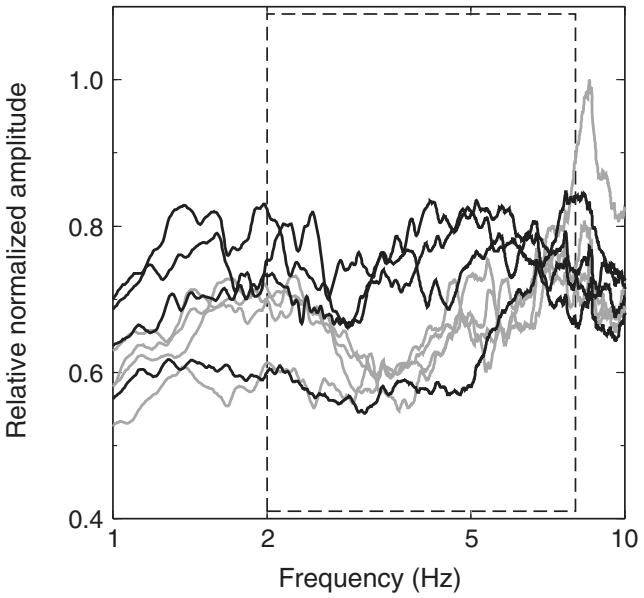

Figure 4. Relative noise spectra at eight OBSs within the two boxes in Figure 1b. The gray lines correspond to the noise spectra at OBSs indicated by circles within the left box in Figure 1b. The black lines represent those at OBSs indicated by triangles within the right box in Figure 1b. The region within the dashed-line box indicates the frequency band of 2–8 Hz.

waves are excited incessantly by local microseisms and/or small-sized earthquakes in the NFZ and propagate in the accretionary prism to obscure the *P* waves of near-field earthquakes.

Selection of *P* Waveforms

We used *P* waveforms for events that mainly occurred near the NFZ. Obana *et al.* (2015) indicated that earthquakes along the fault zone occurred in both the oceanic crust and uppermost mantle. When *P* waveforms from earthquakes occurring within the oceanic crust are used, extra care should be exercised because the wavetrain can have multiple phases due to different propagation paths. The occurrence of multiple *P* paths depends on the source mechanism, epicentral distance, and focal depth relative to the Moho depth near the source. In this study, we selected only impulsive *P* waves (Fig. 5) in order to avoid significant contaminations of multipath *P* waves.

Ps-Converted Wave Observation

In this study, we focus only on the regions near the NFZ and the array area west of the deformation front. Figure 5 shows waveform examples of *P* and *Ps* waves at stations S005, S008, and S025. Stations of S008 and S025 are located on the NFZ, and the other station of S005 is farther south but west of the deformation front (Fig. 1b). As shown in Figure 5b, c,e,f,h,i, the horizontal components clearly display the first *Ps*-converted waves 1–2 s after the *P* arrival with a similar slowness to that of the *P* wave. *Ps* delay times of 1–2 s and around 2 s could be observed at stations east and west

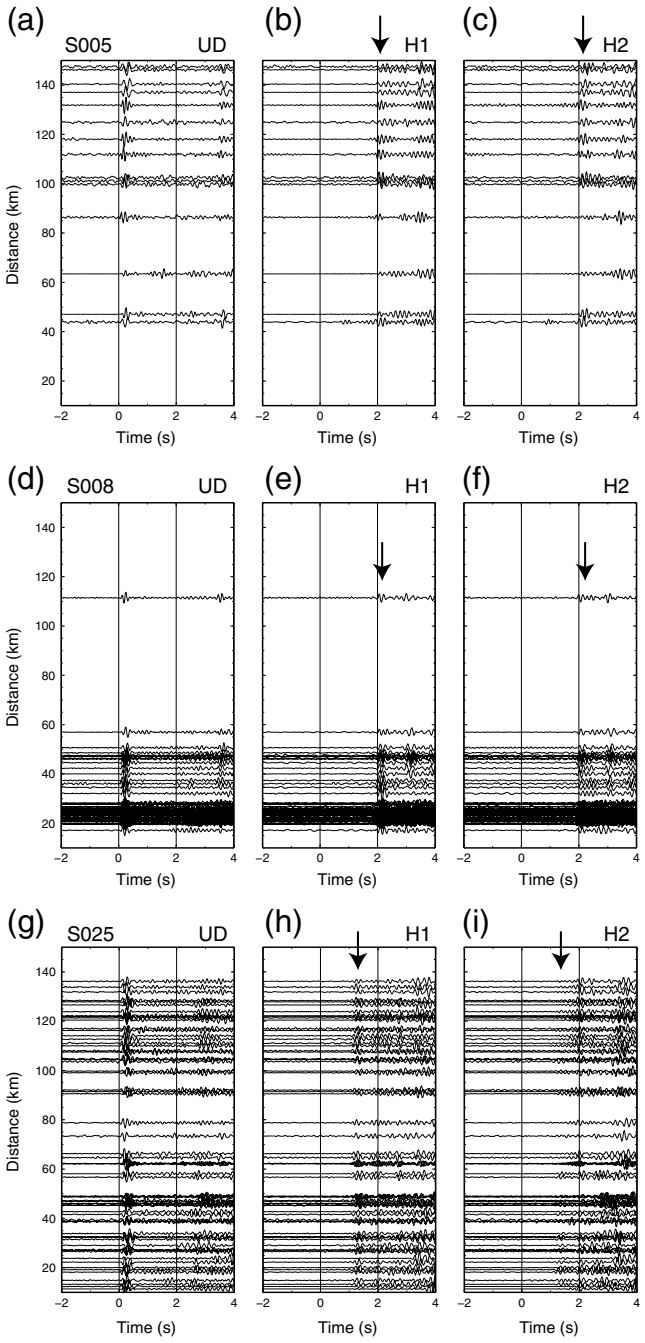

Figure 5. Waveform examples of *P* and *Ps* waves at 2–8 Hz frequencies. (a) Waveforms in the vertical component at station S005 as a function of the epicentral distance, which are aligned by handpicked *P* arrival times. Zero time indicates the *P* arrival time. (b,c) Same as (a) but for the horizontal components H1 and H2. The arrows indicate the *Ps* arrivals. (d–f) Same as (a–c) but at station S008. (g–i) Same as (a–c) but at station S025.

of the deformation front, respectively. These waveforms also appear to show the secondary and later *Ps*-converted waves, which potentially originate from deeper seismic interfaces.

We think that the *Ps* wave in our observations, which arrived earliest after the *P* wave with a differential travel time of 1–2 s, is generated primarily at the base of the sediment

layer (top of oceanic crust), because this interface has the largest impedance contrast below the seafloor according to multichannel seismic (MCS) reflection results relevant to the Juan de Fuca plate west of the deformation front (e.g., Yuan *et al.*, 1994; Hasselgren and Clowes, 1995; Nedimović *et al.*, 2009). Because we did not use the SeaJade data to estimate velocity models in this region, we can only use the differential travel time to infer that the conversion is indeed at the sediment–basement interface.

MCS reflection surveys indicate that the sedimentary sequence on the northern Juan de Fuca plate is generally flat-lying and undisturbed. Its thickness in this region varies from 200 m in the western part of the plate to 1600 m in the eastern part (Hasselgren and Clowes 1995) and becomes 2.0–2.5 km just seaward of the deformation front (Yuan *et al.*, 1994). Dash and Spence (2011) reported that V_P and V_S for unconsolidated sediments with no hydrates or free gas are 1.6–1.8 km s^{-1} and 0.3–0.8 km s^{-1}, respectively. Ruan *et al.* (2014) reported similar V_S values for the sediment on the Juan de Fuca plate. Riedel *et al.* (2014) reported V_S values of up to 0.7 km s^{-1} in the upper 300 m at the first frontal thrust fault east of the deformation front. Based on these previous studies, we used a V_P of 1.7 km s^{-1} and V_S of 0.7 km s^{-1}. The obtained converted depths of 1.19 and 2.38 km, for *P–Ps* differential travel times 1 and 2 s, respectively, are consistent with previously reported depths of the sediment base.

Processing

Estimation of the OBS Orientation for Isotropic and Anisotropic Cases

In this section, we describe how we determine both the horizontal orientation of OBSs and the fast polarization direction within marine sediments using *Ps* waves converted at the sediment–basement interface. If the sediment layer is isotropic, it is straightforward to estimate the horizontal orientation of the OBS. For each earthquake, *P* and *Ps* waves appear in the vertical and radial (i.e., epicenter to OBS) components, respectively. Therefore, by synthesizing the waveform for every direction and by multiplying the two horizontal components with the rotation matrix, we can determine the radial direction in which the cross-correlation coefficient between the *P* and the *Ps* waves is maximum (Fig. 2b). Using the back-azimuth (BAZ) information, the horizontal orientation of OBS can be estimated on the basis of the radial direction. However, if the marine sediment is anisotropic, *Ps* wave converted at the base of marine sediments is split into fast and slow polarization axes (Fig. 2c). In such a case, we can correct the split *Ps* wave using splitting parameters; that is, the differential travel time δt between fast and slow shear waves and the direction θ at which the cross-correlation coefficient between the two horizontal components is maximum. Because the corrected particle motion of the *Ps* wave is primarily in the radial direction, as will be verified in the Synthetic Tests section, the horizontal orientation of the OBS can be estimated in the same way as for isotropic sediment.

Procedure of Estimating OBS Horizontal Orientation and Fast Polarization Direction

Step 1: Estimation of the Splitting Parameters δt and θ

The horizontal component H1 is in the direction φ (unknown parameter), measured clockwise from north (Fig. 2d), and H2 = H1 + $\pi/2$. First, we can estimate the splitting parameters δt and θ using the traditional cross-correlation method with a grid search (Bowman and Ando, 1987). The time window is 0.5 s from the handpicked *Ps* arrival time, and the search range of δt is −0.06 to 0.06 s for the H2 component relative to the H1 component. This time-window range was determined by checking several events at every OBS site. When $C_1 > 0.9$ and $|\delta t| > 0.01$ s, in which C_1 is the cross-correlation coefficient, we can correct the particle motion of *Ps* waves by rotating the waveforms by θ from H1/H2 to H1′/H2′ and time-shifting H2′ by δt. The material beneath a station is considered isotropic if $C_1 > 0.9$ and $|\delta t| \leq 0.01$ s. We use the waveform data to estimate the horizontal orientation of the OBS only.

Step 2: Estimation of the Direction of the Corrected *Ps* wave

H1′ is now oriented at $\varphi + \theta$. If δt is positive, H1′ is the fast polarization direction, and vice versa. The corrected particle motion defined by H1′ and H2′ should be almost linear because we have selected *Ps* waveforms with $C_1 > 0.9$. We can then solve the eigenvalue problem with respect to the particle motion in the H1′ and H2′ systems. The first eigenvector with the largest eigenvalue represents the primary direction of the particle motion of the *Ps* wave. Using the H1′ and H2′ components of the first eigenvector v_1 and v_2, the angle ξ between the azimuth of the particle motion and H1′ can be estimated from the following relation (Fig. 2e):

$$\xi = \arctan(v_2/v_1). \tag{1}$$

Thus, the direction of the corrected *Ps* wave can be described by $\varphi + \theta + \xi$. Using the estimated eigenvalues λ_1 and λ_2, the degree of rectilinearity L of the particle motion can be described by

$$L = 1 - (\lambda_2/\lambda_1) \tag{2}$$

(Jurkevics, 1988). If $L < 0.90$, we discard the waveform.

Step 3: Determination of the Two Directions

The BAZ ψ of an event is also measured clockwise from north. A key point is that the direction $\varphi + \theta + \xi$ discussed above inherently corresponds to either ψ or $\psi + \pi$. To remove the ambiguity of π, we can use the cross-correlation coefficient

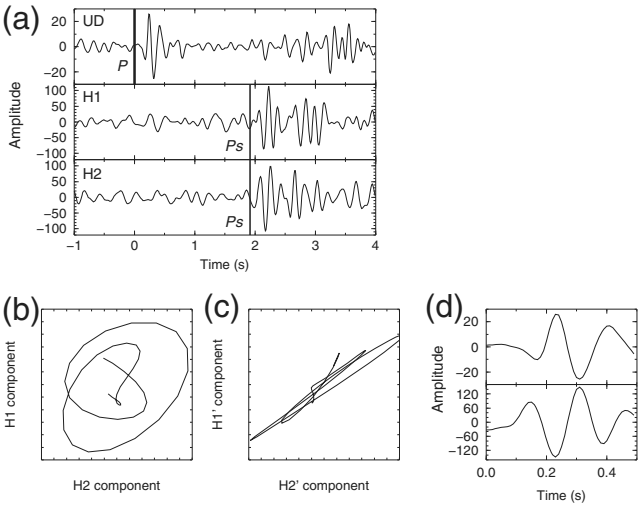

Figure 6. Waveform examples for estimating the orientation of OBS and fast polarization directions. (a) Three-component waveform for an earthquake recorded at S008. The handpicked times of *P* and *Ps* waves are denoted by *P* in the vertical component and *Ps* in the horizontal components. (b) Particle motion of the *Ps* wave in (a) with a time window of 0.5 s from the *Ps* arrival time, as shown in the H1 and H2 components. (c) Particle motion of the corrected *Ps* wave using splitting parameters, as shown in the H1′ and H2′ components. (d) *P* wave (top) and corrected *Ps* wave (bottom) with a time window of 0.5 s from the *P* and *Ps* arrival times.

C_2 between the *P* wave (vertical) and corrected *Ps* wave in the direction of $\varphi + \theta + \xi$. The time window used in the particle motion analysis is 0.5 s for the *P* and *Ps* arrival times, and the search range of the time shift is ±0.15 s. In summary, the following relations can be obtained:

$$\varphi + \theta + \xi = \psi + \pi(C_2 > 0), \tag{3}$$

and

$$\varphi + \theta + \xi = \psi(C_2 < 0). \tag{4}$$

The direction of H1 is represented by φ. The fast polarization direction is described by $\varphi + \theta$ for $\delta t > 0$ s and $\varphi + \theta + \pi/2$ for $\delta t < 0$ s, with δt estimated in step (1). As mentioned above, if $C_1 > 0.9$ and $|\delta t| \leq 0.01$ s, only φ is necessary.

Figure 6 shows the estimated horizontal orientation of the OBS S008 and fast polarization direction for an earthquake at this site with $\psi = 301°$. Using the *Ps* wave emerged in the H1 and H2 components (Fig. 6a), we obtain $\theta = 45.0°$ and $\delta t = 0.05$ s with $C_1 = 0.96$. Figure 6b,c displays the particle motions of the uncorrected and corrected *Ps* waves. The eigenvalue problem in step (2) resulted in $\xi = 37.7°$ and the degree of rectilinearity is 0.98. Because we have obtained in step (3) $C_2 = -0.91$ for the *P* and *Ps* waveforms (Fig. 6d), the directions of H1 and fast polarization calculated with equation (4) are 218° and 263°, respectively.

Synthetic Tests

Here, we demonstrate that the assumption that the corrected particle motion of *Ps* waves corresponds to the radial direction is usually valid. We first examine whether an anisotropic medium with a tilted symmetry axis produces an observable deviation for the corrected particle motion of *Ps* waves (e.g., Savage, 1998; models A–C in Table 1). In addition, we test the following three situations: (1) in model D in Table 1, both *P* and *S* anisotropies are present. *P*-to-*SH* conversion occurs, and the particle motion of *Ps* wave right after the conversion at the sediment–basement interface deviates from the radial direction (Levin and Park, 1997, 1998; Savage, 1998; Liu *et al.*, 2015). (2) Model E in Table 1 features ray bending of direct *P* wave due to seismic-velocity anomalies between sources and receivers (Hu and Menke, 1992), and (3) in model F in Table 1, *Ps* conversion occurs at a dipping sediment–basement interface (Langston, 1977; Cassidy, 1992). These situations potentially give rise to systematic variations of the splitting parameters with BAZs.

To assess the effectiveness of the proposed method and the possible effect of the rotation of particle motion on splitting measurements in situations mentioned above, we conducted a synthetic experiment using a 3D finite-difference approach. The 3D model has rotated staggered grids with second-order calculation accuracies in time and space (Saenger *et al.*, 2000) with time steps of 0.002 s. The model space (x–y–z) was $15 \times 15 \times 25$ km^3 and included four layers with a grid spacing of 0.02 km (Fig. 7a). An absorbing boundary condition was assigned at each side (Clayton and Engquist, 1977) except for the top. The location of the station was set to $(x, y, z) = (7.5, 7.5, 2.0)$ at the model seafloor. Table 2 summarizes the physical parameters of the model. We conducted a total of 24 calculations for each model. For each calculation, we changed the BAZ by 15°, while keeping the depth of the source and its horizontal distance from the center of the model $(x, y) = (7.5, 7.5)$ at 18 and 5.3 km, respectively. Thus, the 24 calculations covered the entire BAZ range of $0° \leq \psi \leq 360°$, as shown in Figure 7b. We applied an explosive source with a Ricker wavelet at a center frequency of 1.96 Hz (maximum frequency of 2.83 Hz) to the source locations. Because the minimum velocity was 1.0 km s^{-1}, the simulation could be conducted under the condition of 17 grids per minimum wavelength at our maximum frequency of 2.83 Hz, which led to sufficiently stable calculations (e.g., Krüger *et al.*, 2005; Bohlen and Saenger, 2006). In the experiments, we set $\varphi = 30°$.

For the sediment layer of models A–C and E–F, we set anisotropies $dV_P = 0\%$ and $dV_S = -4\%$, equivalent to $B = 0\%$ and $E = -4\%$, in which B and E are dimensionless parameters representing anisotropic perturbations of *P* and *S* waves in a weak hexagonal symmetry, respectively (Park and Yu, 1992). For model D, we set $dV_P = -4\%$ and $dV_S = -4\%$ (Fig. 7a; Table 1). Because the delay time is small (<0.07 s), we only considered a weakly anisotropic (4%) sediment layer. The degree of anisotropy in the hexagonal symmetry can be converted to elastic constants (Park and Yu, 1992; Nagaya *et al.*, 2008), and a maximum of 21 elastic constants were incorporated. Table 1 also shows other parameters. S_1 is the azimuth of this axis measured clockwise

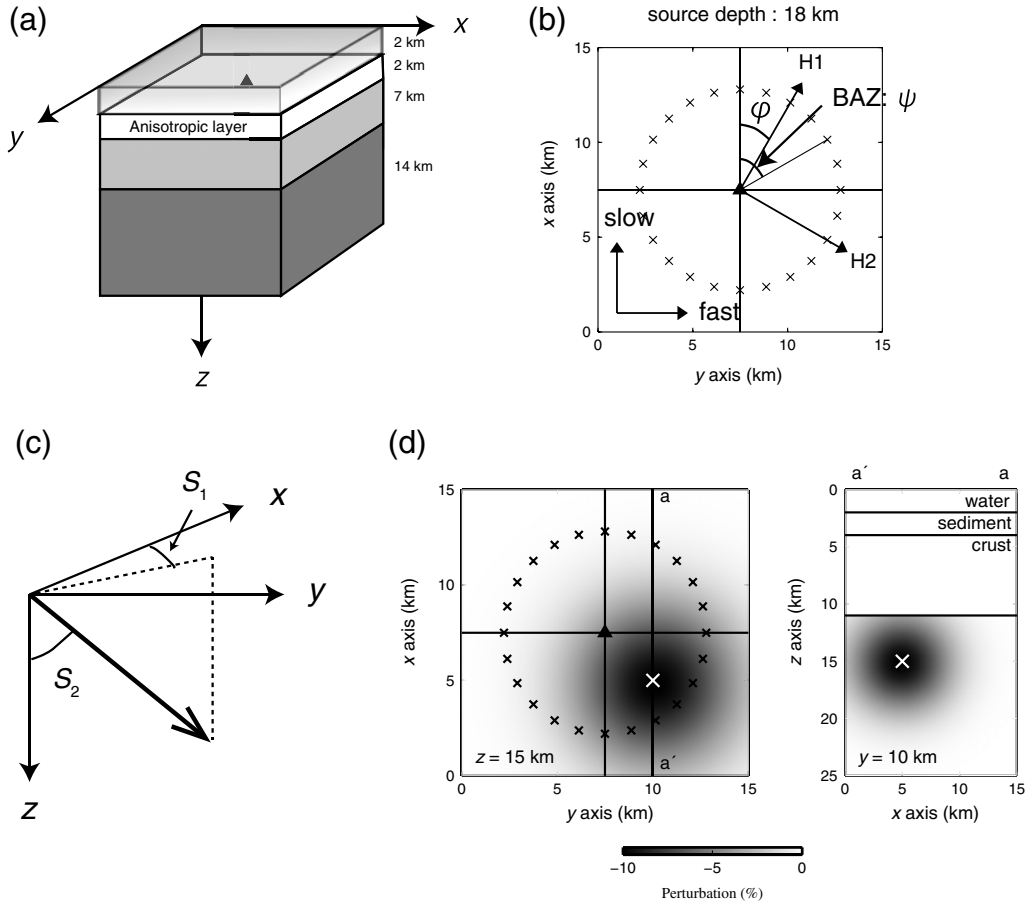

Figure 7. Model space for 3D finite-difference calculation. (a) Model space consisting of water, sediment, crust, and mantle layers. Table 2 summarizes the physical parameters. The sediment layer has $dV_S = -4\%$. Table 1 lists the directions of the symmetry axes. (b) Source locations shown in the x–y domain. The x and y axes correspond to slow and fast polarization directions, respectively, in the sedimentary layer. The definitions of the angles are the same as those in Figure 2. The direction of the H1 component was set to $\varphi = 30°$. (c) S_1 is the azimuth of the hexagonal-symmetry axis measured clockwise from the x direction, and S_2 is the tilt angle of the symmetry axis measured from z direction. (d) (left) An x–y section at $z = 15$ km showing the location of a low-velocity anomaly centered at $(x, y, z) = (5, 10, 15)$ (white cross). The triangle and black crosses indicate the location of the receiver at the seafloor and the source locations at a depth of 18 km, respectively. (right) An x–z section along a–a' in the left panel ($y = 10$ km). The low-velocity anomalies are limited below the depth of 11 km.

from the x direction, and S_2 is the tilt angle of the symmetry axis measured from the downward direction (Fig. 7c). In model E, we assigned a dip of 3° to the sediment–basement interface in order to address the reported dip of the oceanic basement of 3°–4° (Hyndman *et al.*, 1990; Hyndman, 1995) landward of the deformation front off southern Vancouver Island. These parameters represent a sediment layer with a fast axis in the y direction.

Figure 8a shows the three-component synthetic seismograms for model A as a function of ψ, which represents P wave, Ps wave converted at the sediment–basement interface, and Ps wave converted at the crust–mantle boundary (oceanic

Table 1
Parameters of Assumed Anisotropy, Velocity Anomaly, and Sediment Dip in the Synthetic Experiments

	dV_P (%)	dV_S (%)	S_1 (°)	S_2 (°)	dV (%)	Sediment Dip (°)
Model A	0	−4	0	90	0	0
Model B	0	−4	0	70	0	0
Model C	0	−4	0	40	0	0
Model D	−4	−4	0	90	0	0
Model E	0	−4	0	90	−10	0
Model F	0	−4	0	90	0	3

Table 2
Physical Parameters of the Assumed Materials for 3D Synthetic Calculation

	Thickness H (km)	V_P (km s^{-1})	V_S (km s^{-1})	Density ρ (g cm^{-3})
Water	2.00	1.50	0.00	1.00
Sediment	2.00	2.00	1.00	1.91
Crust	7.00	6.27*	3.49	2.78
Mantle	14.00	8.04†	4.47	3.31

*White (1984).
†Dziewonski and Anderson (1981).

Moho) at the theoretical arrival times of 3.12, 4.12, and 5.04 s, respectively. Hereafter, we use the term *Ps* for *Ps* wave converted at the sediment–basement interface. Because upgoing *P* waves go through the seafloor with weak downgoing reflections, resulting in weak multiple reverberations within the sediment, we can isolate the two *Ps*-converted waves. By applying the method to the two waves in time windows 3.1–3.7 s for the *P* wave and 4.1–4.7 s for the *Ps* wave, we estimated the direction of H1, the fast polarization direction, and δt. The search range of the time shift for cross correlation in steps (1) and (3) was within ± 0.3 s.

We applied the proposed method to synthetic waveforms calculated for model A. The estimated fast polarization directions for all the BAZs are estimated to 90° with a sinusoidal fluctuation of $\pm 1°$ (black circles in Fig. 8d). However, for BAZs that coincide with the fast or slow polarization directions (Fig. 8b), no splitting *Ps* waves occur. The H1 directions for all the BAZs sinusoidally fluctuate around 30° by $\pm 3°$ (black circles in Fig. 8b). This implies that the method through steps (1) and (3) can still estimate the H1 direction for anisotropic sediment even if the direction of the incoming *Ps* wave coincides with a polarization direction. Similar results, consistent with the theoretical values, are seen for models B and C that contain an anisotropic sediment layer with the tilted symmetry axes of 70° and 40°, respectively (gray and white circles in Fig. 8b,d). When the hexagonal symmetry axis tilts less than 30° from vertical, the estimated directions tend to be scattered (Nagaya *et al.*, 2008). Moreover, the obtained δt for model A shows good agreement with the theoretical differential time of 0.08 s for BAZs in which the *Ps* wave is split and is 0 s when the BAZ coincides with a polarization direction (black circles in Fig. 8f). For the models of tilted symmetry axes (models B and C in Table 1), the estimated $|\delta t|$ tends to be small and fluctuates with BAZ with smaller S_2 (gray and white circles in Fig. 8f), and $|\delta t|$ is zero if the symmetry axis is vertical. This implies that if *P* and *Ps* waveforms with various BAZs and incidence angles are used, $|\delta t|$ may vary at a single OBS located on the anisotropic sediment with a tilted symmetry axis. The estimates of the H1 direction, fast direction, and $|\delta t|$ for model D, which accounted for the effect of anisotropies dV_P and dV_S, show small deviations from their theoretical values (black circles in Fig. 8c,e,g). Thus, the estimates for models A–D indicate that the deviation of the corrected particle motion of the *Ps* from the radial direction is small.

We also examined a model containing part of a spherical volume of low-seismic velocities in the mantle (Fig. 7d) and anisotropic sediment (model D in Table 1). We set the maximum velocity reduction of $dV = -10\%$ in both the *P* and *S* velocities at the point of $(x, y, z) = (5.0, 10.0, 15.0)$; these perturbations are equivalent to $A = -10\%$ and $D = -10\%$, in which A and D are dimensionless parameters representing isotropic *P* and *S* velocity perturbations, respectively (Park and Yu, 1992). The magnitude of the velocity anomalies is assigned to decrease in a Gaussian distribution from this point to all directions, but the anomaly zone is limited to be below 11 km depth (Fig. 7d). Consequently, both the H1 and fast directions deviate by $\pm 10°$ from the theoretical values, whereas the estimation of the delay time is stable (gray circles in Fig. 8c,e,g). In particular, if the ray path of the direct *P* wave is relatively long and goes through various velocity anomalies to the conversion point, a large deviation in the particle motion from the radial direction may potentially be observed. Furthermore, we examined model F to investigate the effect of a dipping sediment–basement interface on the three measurements. In this model, although $|\delta t|$ is consistent with the theoretical value, the H1 direction and fast direction deviate from the theoretical values by $\pm 12°$ and $\pm 10°$, respectively, and are particularly biased when the BAZ is close to the strike of the dipping interface (white circles in Fig. 8c,e,g).

Determination of OBS Orientations

The final values of the sensor orientation and fast axis at an OBS site can be estimated by averaging those from individual earthquakes. In this study, we use weighted average, with the weight determined from the number of values in each azimuthal bin. Although we use polarity information of *P* and *Ps* waves to determine the H1 direction in step (3), the rose diagram of the estimated sensor orientation shows a small number of directions with the ambiguity of π (Fig. 9). We therefore search the center direction of the azimuthal bin α at a point that maximizes the number of resulting values and then calculate the weighted average and its error within the range of $-\pi/2 < \alpha < \pi/2$. Although we do not consider estimation errors in splitting parameters from the cross-correlation method, such errors can be considered in the weighted average.

From the synthetic tests discussed above, we found that the estimated sensor orientation and fast directions using the

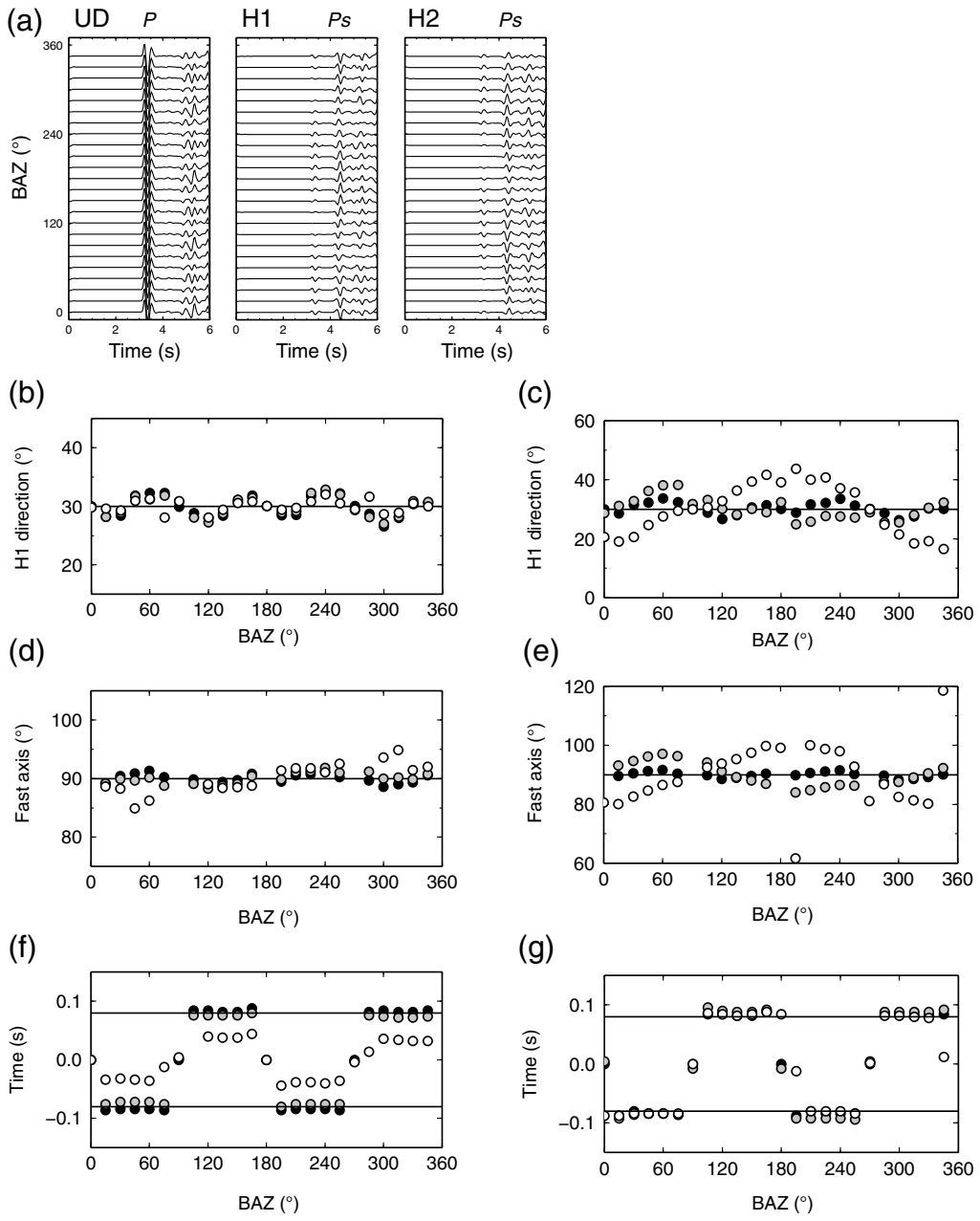

Figure 8. Waveforms and estimated results of synthetic testing, with (b,d,f) for models A (black), B (gray), and C (white), and (c,e,g) for models D (black), E (gray), and F (white). (a) Synthetic waveforms with three components as a function of BAZ. (b,c) Estimated H1 direction as a function of BAZ. The solid line indicates the theoretical value of 30°. The black, gray, and white circles represent the estimated values for models A–C, respectively. (d,e) Estimated fast polarization axis as a function of BAZ. The theoretical value is 90° (solid line). (f,g) Estimated delay time as a function of BAZ. The solid lines indicate the theoretical times of −0.08 and 0.08 s for the anisotropy of $dV_S = -4\%$.

proposed technique may vary with the effects of seismic-velocity anomalies along ray paths and a dipping sediment–basement interface. Although the 1D velocity model used for determining event locations (Obana *et al.*, 2015) potentially causes errors in the direction estimations, the errors seem to be small, as will be discussed in the Confirmation of the Sensor Orientation from *T* Waves section. Therefore, in this study, if errors in either one of these directions are larger than ±10°, we exclude the OBS site from interpreting mechanisms for anisotropic structure. Moreover, to confirm the reliability of the sensor orientations estimates in this study, we compare them with those estimated from *T* waves (Shan *et al.*, 2012). If the difference between the two estimates at an OBS site is larger than 15°, we used what was derived from the *T*-wave analysis to determine the fast direction at that site.

Results

The criteria $C_1 > 0.9$ for the splitting measurements ensures a good signal-to-noise ratio (SNR) of the *Ps* waves,

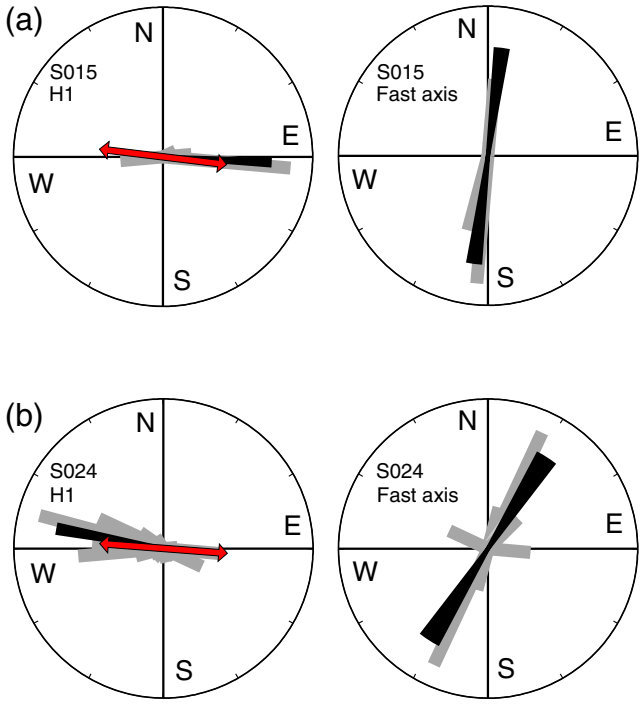

Figure 9. Examples of the estimates of (left) the H1 direction and (right) fast polarization direction for (a) S015 and (b) S024. Gray bars represent the rose diagram. Black fan-shaped sectors show the estimated H1 direction and fast direction with the ambiguity of π. The arc width of each sector indicates the standard deviation of the estimated values. For comparison, double-headed arrows in the left panel represent the H1 direction estimated from Shan *et al.* (2012) using *T*-wave analysis. The color version of this figure is available only in the electronic edition. The color version of this figure is available only in the electronic edition.

defined as the root mean square (rms) amplitude within 0.5 s after the *Ps* arrival (signal part), divided by that before the *P* arrival (noise part). The minimum and median SNRs among all the examined *Ps* waves are 1.8 and 4.3, respectively. Table 3 and Figure 10 present the results for the H1 and fast polarization directions at each OBS site as estimated with the proposed method. We have obtained stable results at 11 OBS sites with errors smaller than ±10°, and scattered results at four OBS sites (S002, S003, S023, and S029; Fig. 10). At some sites, mostly east of the deformation front in the southern part of the array, no clear *P* waves were observed (squares in Fig. 10). At one site (ellipse in Fig. 10a), only the H1 direction can be determined; the marine sediment beneath this OBS is close to isotropic.

When the H1 directions from our method are compared with those from the *T*-wave analysis (Shan *et al.*, 2012), the results at 4 of the 11 OBS sites do not meet the criteria mentioned in the Determination of OBS Orientations section. For these sites, we use the H1 directions from the *T*-wave analysis to determine the fast direction (four arrows in Fig. 10a), and the reliability of the H1 directions at the four sites will be discussed in the Confirmation of the Sensor Orientation from *T* Waves section. Although the H1 directions from the two approaches at the three OBS sites (S009, S014, and S025) differ by less than 45°, they are almost orthogonal at S006. Because the BAZs of the examined events at S006 are limited to only 270°–280°, the estimated H1 direction may be significantly affected by seismic-velocity anomalies along the ray paths of direct *P* waves. Table 3 summarizes the final results, and Figure 11a shows the fast directions. In particular, the sensor orientations at seven OBS sites can be determined without ambiguity (Table 3).

South of the NFZ and west of the deformation front, the fast directions are oriented either northeast–southwest (NE–SW; A in Fig. 11a) or northwest–southeast (NW–SE; D in Fig. 11a). Along the NFZ, the fast directions can be divided into two groups, shown as B1 (NW–SE) and B2 (north-northeast–south-southwest [NNE–SSW]) in Figure 11a.

Confirmation of the Sensor Orientation from *T* Waves

Shan *et al.* (2012) determined the sensor orientation using *T* waves excited by earthquakes, assuming that the *T*-wave particle motion is dominantly in the radial direction from the epicenter to receiver. However, the excitation mechanisms of *T* waves are due mainly to multiple reflections between the downsloping seafloor and the sea surface near the coast, and also rough seafloor scattering above the hypocenter (e.g., Williams *et al.*, 2006). This implies that if the excitation location has a complex bathymetry, the propagation direction of the *T* wave and its particle motion may deviate from the radial direction. Furthermore, if the bathymetry around an OBS is complex, the *T*-wave particle motion may not be oriented in the radial direction. Therefore, we need to check the reliability of the sensor orientation estimated from the *T*-wave analysis.

We first rotate the two horizontal components into north–south and east–west directions using the sensor orientation from Shan *et al.* (2012), and then compare the *T*-wave particle motion at frequencies of 10–20 Hz with the radial direction. We selected waveforms of *T* waves with an SNR greater than 2. The ratio is defined as the rms amplitude within 50 s after the *T* arrival (signal part) divided by that before the *P* arrival (noise part). The first eigenvector of the *T*-wave particle motion is used to determine the dominant particle motion. If the sensor orientation is correct, the *T*-wave particle motion from any earthquake should be oriented in the radial directions. Our comparison indicates that the angular difference between particle motion and the radial direction averaged over all earthquakes is 2.86° ± 2.04° for S006 (15 earthquakes), 4.82° ± 2.78° for S009 (18 earthquakes), 2.16° ± 1.87° for S014 (19 earthquakes), and 2.24° ± 1.55° for S025 (12 earthquakes). Although the angular difference at S009 is less satisfactory than those of the other sites, it seems that the sensor orientations at the four OBS sites estimated by Shan *et al.* (2012) are reliable. The good comparison result also implies that the epicenter locations

Table 3
List of the Ocean-Bottom Seismometer Sensor Orientation (H1) and Fast Polarization Direction

	Estimations from the *Ps*-Converted Phase Method					Final Results	
Station	H1 (°)	Error (°)	Fast Axis (°)	Error (°)	*N* (Events)	H1 (°)	Fast Axis (°)
S002	146.7	18.4	60.5	11.7	3		
S003	253.3	13.8	49.2	7.4	5		
S005	224.3	8.8	47.7	9.4	6	224	48
S006	36.8	1.6	52.0	1.9	14	103 ± 180	119
S007	12.6	1.5	145.7	6.6	4	13	146
S008	198.2	3.3	75.4	1.7	56	198	75
S009	358.6	5.0	116.0	6.0	10	154 ± 180	140
S010	244.7	3.4	156.6	4.2	29	245	157
S012	316.0	1.5	–	–	10		
S014	262.6	7.7	7.2	3.6	13	40 ± 180	137
S015	93.1	1.4	7.6	3.3	12	93	8
S023	145.1	12.1	54.7	12.1	17		
S024	280.6	2.2	32.8	4.8	32	281	33
S025	232.3	1.4	65.7	3.7	46	26 ± 180	11
S028	58.3	7.0	26.7	7.9	7	58	27
S029	233.7	7.9	119.9	14.0	5		

determined by Obana *et al.* (2015) using a 1D velocity model are adequately accurate for our purpose.

Sensitivity

Before we discuss the fast polarization directions obtained in this study, we first estimate the size of the anisotropic rock volume represented by the split *Ps* wave observed at an OBS site. The amplitude of the *Ps* wave observed at a station is constructed by amplitudes that are spread around the ray path. We estimate the horizontal radius of the *Ps* amplitude from the conversion point at the sediment–basement interface using half of a typical wave duration, which we call the sensitivity region R in this study (Fig. 2a). Using the velocity model presented in Table 2 and the method used by Cao and Levander (2010), we numerically estimate R at the sediment base for two earthquakes with a focal depth $H = 30$ km and epicentral distance $\Delta = 40$ km. We first calculate the conversion point at the sediment–basement interface and the travel times of the *Ps* waves that are converted at points scattered nearby. Next, by horizontally moving the scattered point with respect to the conversion point, we search the horizontal distance within which the differential travel time between the *Ps*-converted wave and the *Ps*-scattered wave is less than 0.25 s. The time length of 0.25 s is half of the typical wave duration of the *Ps* phases (Fig. 5). As a result, we obtain $R = 1.003$ km and $R = 1.057$ km at the sediment base on the near and far sides of the earthquake, respectively. Similar results of $R = 0.989$–1.081 km and $R = 1.008$–1.061 km are obtained also for $(\Delta, H) = (100, 30)$ and $(\Delta, H) = (40, 20)$, respectively. These results indicate that R does not depend strongly on event location and probably changes with V_S and the thickness of the sediment. Because the amplitude decreases from the center to the edge within the sensitivity region, the *Ps* amplitude near the conversion point has a large constructive contribution. Considering the above estimations and the case of thicker sediment (e.g., 2 km), the *Ps* waves observed in this study could be affected by the anisotropic structure in the sediment within a horizontal radius of 1 km from an OBS site. Within the volumetric sensitivity region, the *Ps* wave would split because of the anisotropic structure, which is represented by an effective elastic medium containing aligned inclusions such as cracks (e.g., Crampin, 1981).

S Anisotropy

We interpret the observed fast polarization directions west of the deformation front and near the NFZ in the West of the Deformation Front and South of the NFZ and The Nootka Fault Zone sections, respectively. In the Prediction for the Cascadia Basin and Accretionary Prism section, we further speculate on the anisotropic structure within marine sediments of the Cascadia basin and accretionary prism from the results of previous studies.

West of the Deformation Front and South of the NFZ

S anisotropy within marine sediments is created mainly by crack opening and normal faulting associated with the stress field applied to the sediment. In this case, the fast polarization direction is parallel to the compressional direction within the sediment (e.g., Tonegawa, Fukao, Fujie, *et al.*, 2015). When normal faults formed at spreading centers are reactivated such as in the Cascadia basin (Nedimović *et al.*, 2009), *S* anisotropy is also developed in the basement through normal faulting. The basement faulting produces a fast polarization direction parallel to the magnetic lineation.

West of the deformation front, we propose that crack opening is the dominant mechanism for creating *S* anisotropy within the marine sediments (Figs. 11b and 12a). There are not enough earthquakes to constrain the stress field in this

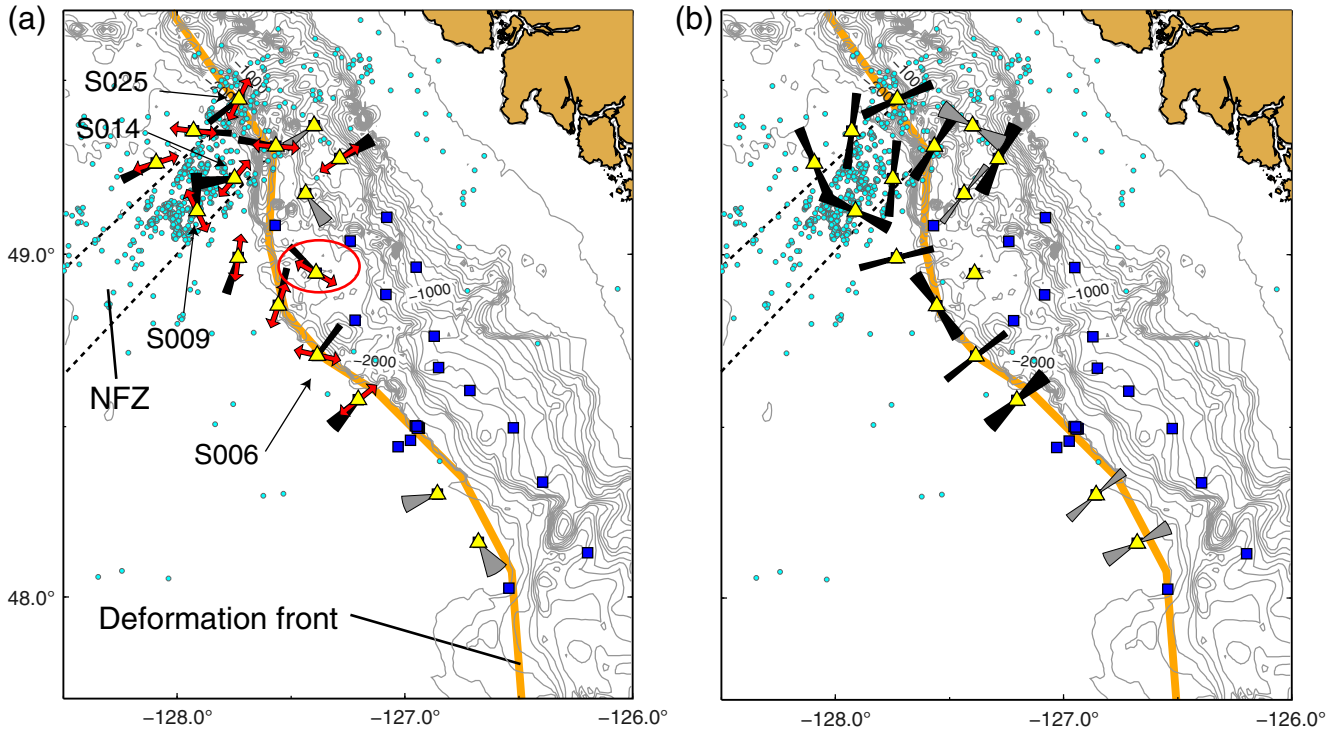

Figure 10. Map showing results obtained using observed waveforms. (a) Fan-shaped sectors show estimated H1 directions at each site from the method devised in this work. The arc width of each sector indicates the standard deviation of the estimated value. Gray sectors indicate large scatter in sensor orientation or fast polarization direction. Dots indicate the locations of earthquakes determined by Obana *et al.* (2015). The OBS sites where the estimation of the sensor orientation or the fast polarization direction is scattered are represented by gray sectors. The ellipse marks the OBS where only the horizontal orientation can be estimated because of isotropic sediment. Double-headed arrow at each station indicates the sensor orientation derived from the linear particle motions of *T* waves (Shan *et al.*, 2012). (b) Estimated fast polarization direction at each OBS site using the proposed method. The color version of this figure is available only in the electronic edition.

region (Fig. 11b). Crack opening may be induced by horizontal compression of sediments across the margin as a result of the Juan de Fuca plate subducting beneath the North American plate in the directions of N56°E–N68°E (DeMets *et al.*, 1990; Riddihough and Hyndman, 1991; region A in Fig. 11b). The fast polarization directions at the two OBSs (S005 and S008; A in Fig. 11a) in this study show good agreement with regard to the convergence direction.

Slightly closer to the deformation front, two other OBS sites S006 and S007 show a NW–SE fast direction (D in Fig. 11a). This fast direction corresponds to the strike direction of the frontal thrusts that have developed due to horizontal compaction (e.g., Westbrook *et al.*, 1994; Yuan *et al.*, 1994).

The Nootka Fault Zone

The OBSs around the NFZ may be divided into two groups (Fig. 11a): (1) a cluster of three showing NW–SE (or north-northwest–south-southeast) fast direction (B1 in Fig. 11a), and (2) another three showing NNE–SSW fast direction (B2 in Fig. 11a). This means that the fast axes within the sediments vary at a scale of ~50 km. As shown in Figure 11b, earthquake focal mechanisms around the NFZ show primarily left-lateral strike-slip faulting. Our estimated fast directions cannot be simply associated with the focal mechanisms. To interpret these fast directions (region B in Fig. 11b), it is necessary to consider the fact that the *S* anisotropic structure in the sediment is potentially affected by fractures and cracks associated with fault motion below (Fig. 12b). On land, characteristic fractures have often been found in the overburden overlying seismically active strike-slip faults. Such fractures are formed before the development of a through-going fault, or *Y* shear (Bartlett *et al.*, 1981), with different direction groups known as Riedel (*R*) shears, antithetic R' shears (e.g., Tchalenko, 1970), *P* shears (Tchalenko and Ambraseys, 1970), and tension fractures (e.g., Wilcox *et al.*, 1973). Similar types of fractures have presumably formed in the marine sediments covering the NFZ. Figure 12b displays theoretically expected fracture directions (e.g., Wilcox *et al.*, 1973; Christie-Blick and Biddle, 1985) with respect to the NFZ. We use the strike direction of the NFZ of N55°E determined from relocated epicenters (Braunmiller and Nábělek, 2002). Although our observations are not completely consistent with the theoretical directions of these shears, group 1 roughly corresponds to antithetic R' shears, and group 2 is close to the orientation of tension fractures.

Because of the lack of large bathymetric relief across the NFZ except for near the Juan de Fuca ridge (Hyndman *et al.*, 1979), we assume that purely left-lateral motion is dominant in the part of the fault zone hosting the six OBSs (B1 and B2 in Fig. 11a). If there is significant transtension or transpres-

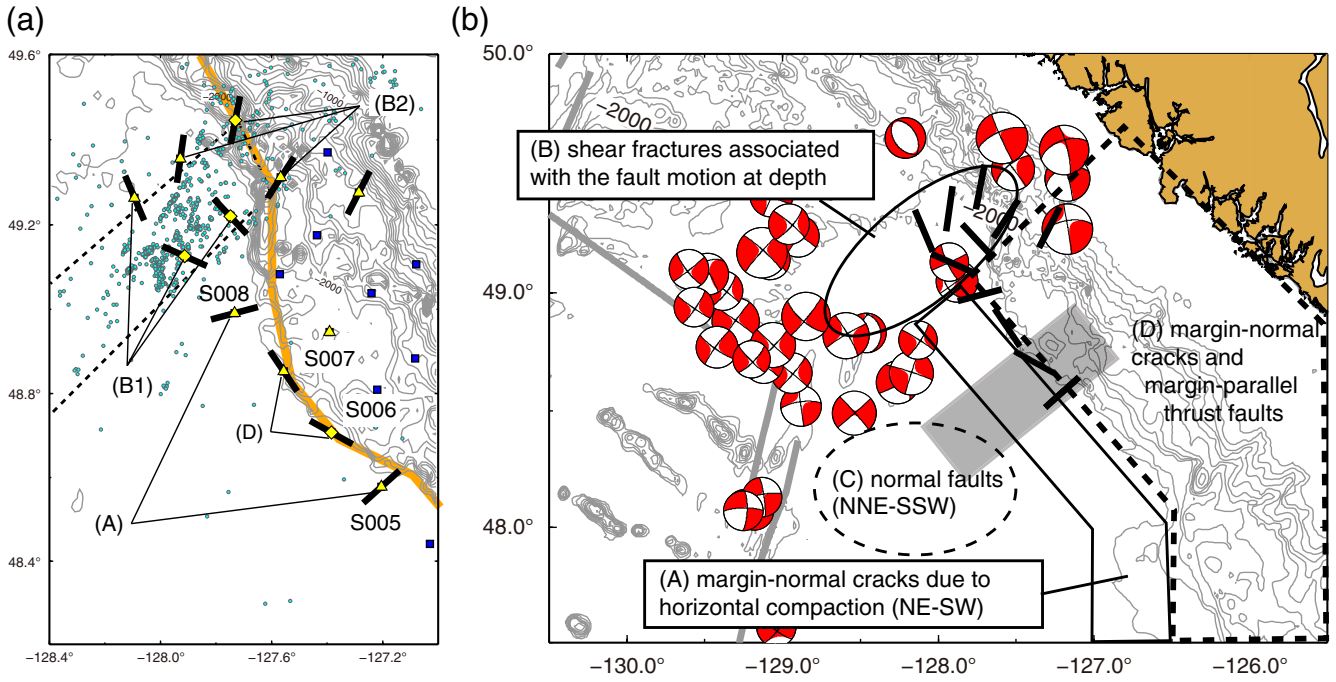

Figure 11. (a) Fast polarization direction at each OBS site as determined using both the proposed method and the *T*-wave analysis of Shan *et al.* (2012). The labels (A, D, B1, and B2) correspond to the four groups of the fast polarization directions. (b) Fracture variations and their directions associated with different mechanisms. The interpretations for the regions A and B are based on our observations, whereas those for the regions C and D are based on results from previous studies. The fast axes at the OBSs within the region A correspond to shear fractures due to Nootka fault motion. Focal mechanism solutions with magnitudes of 5.0 and greater during 2000–2014 are displayed (Ekström *et al.*, 2012). The color version of this figure is available only in the electronic edition.

sion, characteristic pull-apart and push-up structures should form within the shear zone, and the theoretical directions of the shears should be different from those of simple shear (Sanderson and Marchini, 1984). If pull-apart and push-up structures are identified in the existing or future detailed bathymetry maps (e.g., Riedel *et al.*, 2001), it may be necessary to reinterpret the observed fast directions. Although we interpret the fast axes according to cracks and fractures owing to the fault motion at depth in this study, the anisotropic structures within the marine sediment around the NFZ can be due to other mechanisms such as turbidity deposits associated with earthquakes. A more informed interpretation requires integration of information from various disciplines, including seismic surveys, *in situ* stress measurements, and knowledge of sediment dynamics.

Prediction for the Cascadia Basin and Accretionary Prism

Based on results from the previously published studies, we further interpret anisotropic structure in other regions off Vancouver Island outside of the SeaJade study area. In the Cascadia basin, Nedimović *et al.* (2009) reported the existence of steeply dipping normal faults within the sediments due to the reactivation of basement normal faults. Magnetic lineation in the Juan de Fuca plate is oriented mainly NNE–SSW, and the fast polarization direction for the sediment layer appears to be aligned in that direction (region C in Figs. 11b and 12a). In the accretionary prism landward of the deformation front (region D in Fig. 11b), margin-normal cracks have formed due to horizontal compression of sediments, and thrust faults striking at margin-parallel have also been created (e.g., Davis and Hyndman, 1989; Calvert and Clowes, 1990; Hyndman *et al.*, 1990; Westbrook, 1994; Yuan *et al.*, 1994; Fig. 12b). Indeed, a stress field analysis based on the borehole breakouts in the accretionary prism shows nearly margin-normal horizontal compression (N25°–35°E; Riedel *et al.*, 2016). The latter, margin-parallel fast axes, could be inferred in this study in a limited area (Fig. 11a). Therefore, the anisotropic structure in the accretionary prism presumably represents lateral spatial variations of the two effects, as found in the Nankai subduction zone of Japan (e.g., Lin *et al.*, 2010; Tsuji *et al.*, 2011).

Conclusion

Using *Ps* waves converted at the sediment–basement interface, we determined the sensor orientation of OBSs deployed off Vancouver Island. In the meantime, we also determined the fast polarization direction in the sediments from the *Ps*-wave splitting parameters. The validity of this method is confirmed by the use of synthetic waveforms calculated with a 3D finite-difference method. Our numerical simulations also reveal that the estimated sensor orientation from the corrected *Ps* particle motions could be affected by the effects of the dipping symmetry axis of anisotropic structures and seismic-velocity anomalies along the ray paths of direct

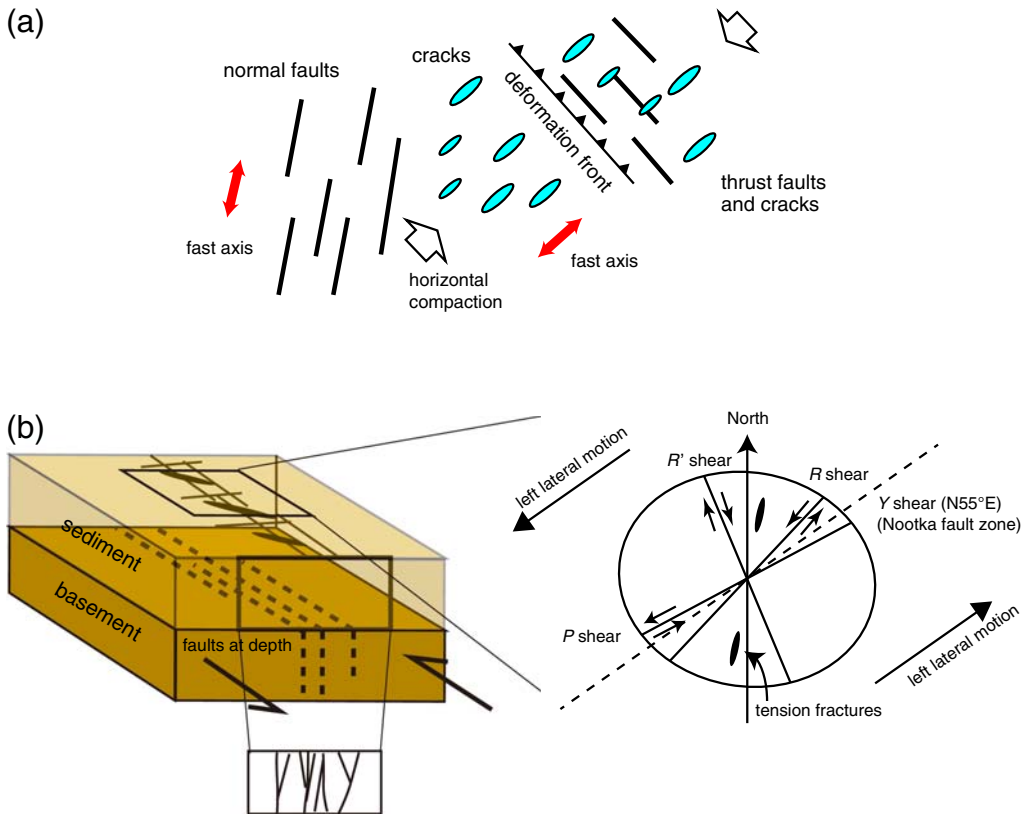

Figure 12. Interpretation of the anisotropic structure within marine sediments off Vancouver Island. (a) Schematic of mechanisms for creating anisotropic structures at different places, relevant to the gray-shaded box in Figure 11b. (b) (left) Schematic of shear fractures within sediments due to fault motion at depth. (right) Angular relation between shears in the sediments associated with the left-lateral motion of the NFZ. The color version of this figure is available only in the electronic edition.

P waves. Accordingly, we corrected the sensor orientations using results of *T*-wave analyses. Thus, this study demonstrates that the technique introduced in this article, when combined with *T*-wave analyses, is an effective tool for estimating the fast directions and sensor orientation when the OBS is located on a seafloor, below which seismic activity in the uppermost mantle is high and the sediment–basement interface is sharp.

The anisotropy of marine sediments determined in this study near the northern Cascadia subduction zone can be interpreted by considering the following two processes: (1) NFZ shearing is thought to be responsible for fractures in the overburden; and (2) horizontal compression near the Cascadia margin due to the subduction of the Juan de Fuca plate is considered to be responsible for margin-perpendicular cracks. From the results of previous studies, two additional factors are expected to contribute to the anisotropy: (1) normal faults associated with the reactivation of fractures within the igneous oceanic crust and (2) Cascadia accretionary prism shortening.

Data and Resources

Seismograms used in this study were collected with ocean-bottom seismometers (OBSs) of Japan Agency for Marine-Earth Science and Technology (JAMSTEC). Figures were created using the Generic Mapping Tools v.4.5.7 (http://gmt.soest.hawaii.edu/, last accessed March 2016).

Acknowledgments

We thank R. Hyndman for his constructive comments that improved the article. We also acknowledge helpful and detailed reviews from Jeffrey Park and an anonymous reviewer. This study was partially supported by the Japan Society for the Promotion of Science (JSPS) (23253005). T. T. was funded by a Research Fellowship of the JSPS for Grants-in-Aid for Young Scientists (B) (15K17753). This article is also the Geological Survey of Canada Contribution Number 20160105.

References

Bartlett, W. L., M. Friedman, and J. M. Logan (1981). Experimental folding and faulting of rocks under confining pressure, *Tectonophysics* **79,** 255–277.

Bird, P. (2003). An updated digital model of plate boundaries, *Geochem. Geophys. Geosyst.* **4,** no. 3, 1027, doi: 10.1029/2001GC000252.

Bohlen, T., and E. Saenger (2006). Accuracy of heterogeneous staggered-grid finite difference modeling of Rayleigh waves, *Geophysics* **71,** T109–T115.

Bowman, J. R., and M. Ando (1987). Shear-wave splitting in the upper-mantle wedge above the Tonga subduction zone, *Geophys. J. Int.* **88,** no. 1, 25–41.

Braunmiller, J., and J. Nábělek (2002). Seismotectonics of the Explorer region, *J. Geophys. Res.* **107,** no. B10, 2208, doi: 10.1029/2001JB000220.

Butler, R. (2006). Observations of polarized seismoacoustic T waves at and beneath the seafloor in the abyssal Pacific ocean, *J. Acoust. Soc. Am.* **120,** no. 6, 3599–3606.

Calvert, A. J., and R. M. Clowes (1990). Deep, high-amplitude reflections from a major shear zone above the subducting Juan de Fuca plate, *Geology* **18,** 1091–1094.

Cao, A., and A. Levander (2010). High-resolution transition zone structures of the Gorda slab beneath the western United States: Implication for deep water subduction, *J. Geophys. Res.* **115,** no. B07301, doi: 10.1029/2009JB006876.

Cassidy, J. F. (1992). Numerical experiments in broadband receiver functions analysis, *Bull. Seismol. Soc. Am.* **82,** 1453–1474.

Christie-Blick, N., and K. T. Biddle (1985). Deformation and basin formation along strike-slip faults, in *Strike-Slip Deformation, Basin Formation, and Sedimentation*, K. T. Biddle and N. Christie-Blick (Editors), Society of Economic Paleontologists and Mineralogists Special Publication, Tulsa, Oklahoma, Vol. 37, 1–34.

Clayton, R., and B. Engquist (1977). Absorbing boundary condition for acoustic and elastic wave equations, *Bull. Seismol. Soc. Am.* **67,** 1529–1540.

Crampin, S. (1981). A review of wave motion in anisotropic and cracked elastic-media, *Wave Motion* **3,** 343–391.

Dash, R., and G. Spence (2011). *P*-wave and *S*-wave velocity structure of northern Cascadia margin gas hydrates, *Geophys. J. Int.* **187,** 1363–1377, doi: 10.1111/j.1365-246X.2011.05215.x.

Davis, E. E., and R. D. Hyndman (1989). Accretion and recent deformation of sediments along the northern Cascadia subduction zone, *Geol. Soc. Am. Bull.* **101,** 1465–1480.

DeMets, C., R. G. Gordon, D. F. Argus, and S. Stein (1990). Current plate motions, *Geophys. J. Int.* **101,** 423–478.

Duennebier, F. K., P. N. Anderson, and G. J. Fryer (1987). Azimuth determination of and from horizontal ocean bottom seismic sensors, *J. Geophys. Res.* **92,** no. B5, 3567–3572.

Dziewonski, A. D., and D. L. Anderson (1981). Preliminary reference Earth model, *Phys. Earth Planet. In.* **25,** 297–356.

Ekström, G., M. Nettles, and A. M. Dziewoński (2012). The global CMT project 2004–2010: Centroid-moment tensors for 13,017 earthquakes, *Phys. Earth Planet. In.* **200/201,** 1–9.

Ewing, M., W. S. Jardetzky, and F. Press (1957). *Elastic Waves in Layered Media*, McGraw-Hill, New York, New York, 1–380.

Fujie, G., S. Kodaira, M. Yamashita, T. Sato, T. Takahashi, and N. Takahashi (2013). Systematic changes in the incoming plate structure at the Kuril trench, *Geophys. Res. Lett.* **40,** 88–93, doi: 10.1029/2012GL054340.

Haacke, R. R., and G. K. Westbrook (2006). A fast, robust method for detecting and characterizing azimuthal anisotropy with marine *PS* converted waves, and its application to the west Svalbard continental slope, *Geophys. J. Int.* **167,** 1402–1412, doi: 10.1111/j.1365-246X.2006.03186.x.

Haacke, R. R., G. K. Westbrook, and S. Peacock (2009). Layer stripping of shear-wave splitting in marine *PS* waves, *Geophys. J. Int.* **176,** 782–804, doi: 10.1111/j.1365-246X.2008.04060.x.

Hasselgren, E. O., and R. M. Clowes (1995). Crustal structure of northern Juan de Fuca plate from multichannel reflection data, *J. Geophys. Res.* **100,** no. B4, 6469–6486.

Hu, G., and W. Menke (1992). Formal inversion of laterally heterogeneous velocity structure from *P*-wave polarization data, *Geophys. J. Int.* **110,** 63–69.

Hyndman, R. D. (1995). The lithoprobe corridor across the Vancouver Island continental margin: The structural and tectonic consequences of subduction, *Can. J. Earth Sci.* **32,** 1777–1802.

Hyndman, R. D., R. P. Riddihough, and R. Herzer (1979). The Nootka fault zone—A new plate boundary off western Canada, *Geophys. J. Roy. Astron. Soc.* **58,** 667–683.

Hyndman, R. D., C. J. Yorath, R. M. Clowes, and E. E. Davis (1990). The northern Cascadia subduction zone at Vancouver Island: Seismic structure and tectonic history, *Can. J. Earth Sci.* **27,** 313–329.

Jurkevics, A. (1988). Polarization analysis of three-component array data, *Bull. Seismol. Soc. Am.* **78,** no. 5, 1725–1743.

Kibblewhite, A. C., and K. C. Ewans (1986). Wave–wave interactions, microseisms, and infrasound ambient noise in the ocean, *J. Acoust. Soc. Am.* **78,** 981–994.

Krüger, O. S., E. H. Saenger, and S. A. Shapiro (2005). Scattering and diffraction by a single crack: An accuracy analysis of the rotated staggered grid, *Geophys. J. Int.* **162,** 25–31.

Langston, C. (1977). The effect of planar dipping structure on source and receiver response for constant ray parameter, *Bull. Seismol. Soc. Am.* **67,** no. 4, 1029–1050.

Leahy, G. M., J. A. Collins, C. J. Wolfe, G. Laske, and S. C. Solomon (2010). Underplating of the Hawaiian Swell: Evidence from teleseismic receiver functions, *Geophys. J. Int.* **183,** 313–329.

Levin, V., and J. Park (1997). *P–SH* conversions in a flat-layered medium with anisotropy of arbitrary orientation, *Geophys. J. Int.* **131,** 253–266.

Levin, V., and J. Park (1998). *P–SH* conversions in layered media with hexagonally symmetric anisotropy: A cookbook, *Pure Appl. Geophys.* **151,** 669–697.

Lin, W., M. Doan, J. C. Moore, L. McNeill, T. B. Byrne, T. Ito, D. Saffer, M. Conin, M. Kinoshita, Y. Sanada, *et al.* (2010). Present-day principal horizontal stress orientations in the Kumano forearc basin of the southwest Japan subduction zone determined from IODP NanTroSEIZE drilling Site C0009, *Geophys. Res. Lett.* **37,** L13303, doi: 10.1029/2010GL043158.

Liu, Z., J. Park, and D. M. Rye (2015). Crustal anisotropy in northeastern Tibetan plateau inferred from receiver functions: Rock textures caused by metamorphic fluids and lower crust flow?, *Tectonophysics* **661,** 66–80, doi: 10.1016/j.tecto.2015.08.006.

Longuet-Higgins, M. S. (1950). A theory of the origin of microseisms, *Phil. Trans. Roy. Soc. Lond. A* **243,** 1–35, doi: 10.1098/rsta.1950.0012.

Müller, R. D., M. Sdrolias, C. Gaina, and W. R. Roest (2008). Age, spreading rates, and spreading asymmetry of the world's ocean crust, *Geophys. Geophys. Geosyst.* **9,** no. Q04006, doi: 10.1029/2007GC001743.

Nagaya, M., H. Oda, H. Akazawa, and M. Ishise (2008). Receiver functions of seismic waves in layered anisotropic media: Application to the estimate of seismic anisotropy, *Bull. Seismol. Soc. Am.* **98,** no. 6, 2990–3006.

Nedimović, M. R., D. R. Bohnenstiehl, S. M. Carbotte, J. P. Canales, and R. P. Dziak (2009). Faulting and hydration of the Juan de Fuca plate system, *Earth Planet. Sci. Lett.* **284,** 94–102.

Obana, K., M. Scherwath, Y. Yamamoto, S. Kodaira, K. Wang, G. Spence, M. Riedel, and H. Kao (2015). Earthquake activity in northern Cascadia subduction zone off Vancouver Island revealed by ocean-bottom seismograph observations, *Bull. Seismol. Soc. Am.* **105,** no. 1, 489, doi: 10.1785/0120140095.

Park, J., and Y. Yu (1992). Anisotropy and coupled free oscillations: Simplified models and surface waves observations, *Geophys. J. Int.* **110,** 401–420.

Riddihough, R. (1984). Recent movements of the Juan de Fuca plate system, *J. Geophys. Res.* **89,** no. B8, 6980–6994.

Riddihough, R. P., and R. D. Hyndman (1991). The modern plate tectonic regime of the continental margin of western Canada, in *Geology of the Cordilleran Orogen in Canada*, H. Gabrielse and C. J. Yorath (Editors), Vol. 2, Geol. Surv. Can., Geology of Canada, 437–455.

Riedel, M., D. Goldberg, and G. Guerin (2014). Compressional and shear-wave velocities from gas hydrates bearing sediments: Examples from the India and Cascadia margins as well as Arctic permafrost regions, *Mar. Petrol. Geol.* **58,** 292–320, doi: 10.1016/j.marpetgeo.2014.07.028.

Riedel, M., D. S. Kelly, J. R. Delaney, G. D. Spence, R. D. Hyndman, L. A. Mayer, B. Calder, M. D. Lilley, H. C. Olson, M. O. Schrenk, *et al.* (2001). Discovery of an active submarine mud volcano along the Nootka fault west of Vancouver Island, presented at *2001 Fall Meeting, AGU*, San Francisco, California, 10–14 December, Abstract OS12B-0428.

Riedel, M., K. Naegeli, and M. Côté (2016). Assessment of submarine slope failures off Vancouver Island, British Columbia, *Geol. Surv. Canada Open-File 8008*, doi: 10.4095/297904, 108 pp.

Ruan, Y., D. W. Forsyth, and S. W. Bell (2014). Marine sediment shear velocity structure from the ratio of displacement to pressure of Rayleigh

waves at seafloor, *J. Geophys. Res.* **119,** 6357–6371, doi: 10.1002/2014JB011162.

Saenger, E. H., N. Gold, and S. A. Shapiro (2000). Modeling the propagation of elastic waves using a modified finite-difference grid, *Wave Motion* **32,** 77–92.

Sanderson, D. J., and W. R. D. Marchini (1984). Transpression, *J. Struct. Geol.* **6,** no. 5, 449–458.

Savage, M. K. (1998). Lower crustal anisotropy or dipping boundaries? Effects on receiver functions and a case study in New Zealand, *J. Geophys. Res.* **103,** no. B7, 15,069–15,087.

Scherwath, M., G. Spence, K. Obana, S. Kodaira, K. Wang, M. Riedel, J. McGuire, and J. Collins (2011). Seafloor seismometers monitor northern Cascadia earthquakes, *Eos Trans. AGU* **92,** no. 47, 421–422, doi: 10.1029/2011EO470001.

Shan, S., H. Kao, and K. Obana (2012). Structural characteristics of the northern Cascadia deformation front: Preliminary result of SeaJade Experiment, presented at *2012 Fall Meeting, AGU*, San Francisco, California, 3–7 December, Abstract T22D-04.

Smith, W. H. F., and D. T. Sandwell (1997). Global sea floor topography from satellite altimetry and ship depth soundings, *Science* **277,** 1956, doi: 10.1126/science.277.5334.1956.

Stachnik, J. C., A. F. Sheehan, D. W. Zietlow, Z. Yang, J. Collins, and A. Ferris (2012). Determination of New Zealand ocean bottom seismometer orientation via Rayleigh-wave polarization, *Seismol. Res. Lett.* **83,** no. 4, 704–713, doi: 10.1785/0220110128.

Tchalenko, J. S. (1970). Similarities between shear-zones of different magnitudes, *Geol. Soc. Am. Bull.* **81,** 1625–1640.

Tchalenko, J. S., and N. N. Ambraseys (1970). Structural analysis of the Dasht-e Bayaz (Iran) earthquake fractures, *Geol. Soc. Am. Bull.* **81,** 41–60.

Tonegawa, T, Y. Fukao, G. Fujie, S. Takemura, T. Takahashi, and S. Kodaira (2015). Geographical distribution of shear wave anisotropy within marine sediments in the northwestern Pacific, *Prog. Earth Planet. Sci.* **2,**27, doi: 10.1186/s40645-015-0057-2.

Tonegawa, T., Y. Fukao, T. Takahashi, K. Obana, S. Kodaira, and Y. Kaneda (2015). Ambient seafloor noise excited by earthquakes in the Nankai subduction zone, *Nat. Comm.* **6,** 6132, doi: 10.1038/ncomms7132.

Tsuji, T., J. Dvorkin, G. Mavko, N. Nakata, T. Matsuoka, A. Nakanishi, S. Kodaira, and O. Nishizawa (2011). V_P/V_S ratio and shear-wave splitting in the Nankai trough seismogenic zone: Insights into effective stress, pore pressure, and sediment consolidation, *Geophysics* **76,** no. 3, WA71–WA82.

Webb, S. C. (1998). Broadband seismology and noise under the ocean, *Rev. Geophys.* **36,** no. 1, 105–142.

Westbrook, G. K. (1994). Growth of accretionary wedges off Vancouver Island and Oregon, in *Proc. of the Ocean Drilling Program*, Initial Reports 146, G. K. Westbrook, B. Carson, R. J. Musgrave, J. Ashi, B. Baranov, K. M. Brown, A. Camerlenghi, J. Caulet, N. Chamov, and M. B. Clennell, *et al.* (Editors), Ocean Drilling Program, College Station, Texas, 381–388.

Westbrook, G. K., B. Carson, and Shipboard Scientific Party (1994). Summary of Cascadia drilling results, in *Proc. of the Ocean Drilling Program*, Initial Reports 146, G. K. Westbrook, B. Carson, R. J. Musgrave, J. Ashi, B. Baranov, K. M. Brown, A. Camerlenghi, J. Caulet, N. Chamov, and M. B. Clennell, *et al.* (Editors), Ocean Drilling Program, College Station, Texas, 389–396.

White, R. S. (1984). Atlantic Ocean crust: Seismic structure of a slow spreading ridge, in *Ophiolites and Oceanic Lithosphere*, I. Gass, S. Lippard, and A. Shelton (Editors), Geil. Soc. Lond. Spec. Pub., Vol. 13, Geological Society of London, London, 101–111.

Wilcox, R. E., T. P. Handing, and D. R. Seely (1973). Basic wrench tectonics, *Am. Assoc. Petrol. Geol.* **57,** no. 1, 74–96.

Williams, C. M., R. A. Stephen, and D. K. Smith (2006). Hydroacoustic events located at the intersection of the Atlantis (30° N) and Kane (23°40′ N) transform faults with the mid-Atlantic ridge, *Geochem. Geophys. Geosyst.* **7,** no. Q06015, doi: 10.1029/2005GC001127.

Wolfe, C. J., S. C. Solomon, G. Laske, J. A. Collins, R. S. Detrick, J. A. Orcutt, D. Bercovici, and E. H. Hauri (2009). Mantle shear-wave velocity structure beneath the Hawaiian hot spot, *Science* **326,** 1388, doi: 10.1126/science.1180165.

Yuan, T., G. D. Spence, and R. D. Hyndman (1994). Seismic velocities and inferred porosities in the accretionary wedge sediments at the Cascadia margin, *J. Geophys. Res.* **99,** no. B3, 4413–4427.

Zha, Y., S. C. Webb, and W. Menke (2013). Determining the orientations of ocean bottom seismometers using ambient noise correlation, *Geophys. Res. Lett.* **40,** 1–6, doi: 10.1002/grl.50698.

Research and Development Center for Earthquake and Tsunami
Japan Agency for Marine-Earth Science and Technology
3173-25, Showa-machi, Kanazawa-ku
Yokohama 236-0001, Japan
tonegawa@jamstec.go.jp
(T.T., K.O., Y.Y., S.K.)

Pacific Geoscience Centre
Geological Survey of Canada
Natural Resources Canada
Sidney, British Columbia
Canada V8L 4B2
(K.W., H.K.)

GEOMAR Helmholtz Centre for Ocean Research Kiel
Wischhofstraße 1-3
D-24148 Kiel, Germany
(M.R.)

School of Earth and Ocean Sciences
University of Victoria
Victoria, British Columbia
Canada V8W 3V6
(G.S.)

Manuscript received 16 March 2016;
Published Online 15 November 2016